Energy Conversion and Management: X 30 (2026) 101633

Contents lists available at ScienceDirect

Energy Conversion and Management: X

journal homepage: www.sciencedirect.com/journal/energy-conversion-and-management-x

Wind variability and its effect on transmission line capacity estimation

Nika Mlinarič Hribar [a,b,*], Matjaž Depolli [a], Gregor Kosec [a]

[a] Jožef Stefan Institute, Jamova cesta 39, Ljubljana, 1000, Ljubljana, Slovenia
[b] Jožef Stefan International Postgraduate School, Jamova cesta 39, Ljubljana, 1000, Ljubljana, Slovenia

ARTICLE INFO

Keywords:
Power grid operation
Transmission line
Dynamic thermal rating
Ampacity
Wind variability

ABSTRACT

Transmission line ampere capacity, i.e. ampacity, can be determined in real time using dynamic thermal rating (DTR). Standard DTR systems rely on weather data averaged over multi-minute windows. While sufficient for most weather parameters, this approach can introduce considerable inaccuracies due to short-term variability of both wind speed and direction.

This study investigates the inaccuracies using high-resolution (1-second) wind measurements from an in-service transmission line. We evaluate two commonly used wind-averaging methods and show that variability in wind direction and the relative angle of wind crucially influence the results. In spans with parallel wind, which are often critical spans, i.e. spans that limit the ampacity of the whole line, averaged data commonly underestimates ampacity by more than 10%, with the maximum observed underestimation being over 45%. On the other hand, in perpendicular wind scenarios, averaging may lead to overestimation (by up to 25%), raising operational safety concerns.

For transmission system operators, incorporating wind-angle sensitivity and leveraging higher-resolution measurements where feasible can improve ampacity accuracy, enhance grid reliability, and unlock additional transfer capacity — contributing to more efficient and secure energy system operation.

1. Introduction

With rising global energy demand and clean energy transition, the energy sector is undergoing a profound transformation, enabled by innovative technology solutions [1–3]. At the level of power grids, specifically the transmission network, the system operators face increasing pressure to increase the capacity, optimise network utilisation and accommodate higher penetrations of variable renewable energy sources. One of the key constraints in this effort is the thermal limit of overhead transmission lines, which must be maintained below critical temperatures to avoid excessive sag and material degradation [4].

The ampere capacity, i.e. ampacity of the line is the maximum permissible current at which this critical temperature is not exceeded. Historically, ampacity was set to a constant value, often referred to as the *static limit*, determined by a set of unfavourable weather conditions (high ambient temperature and solar radiation paired with low wind) [5]. While the use of static limit ensures safe operation under most conditions, it also causes the line to be significantly underutilised most of the time, when the weather conditions are favourable. Furthermore, the static conditions have a small chance of being violated [6], which introduces risks in the operation.

An improvement over the static approach is to monitor the local environmental conditions on a span-by-span basis and adjust ampacity dynamically; this is known as dynamic thermal rating (DTR) [5,7,8]. DTR helps reduce congestion on power lines and optimise their utilisation [9] and is becoming increasingly popular with transmission system operators (TSOs) worldwide.

The capacity of the whole line is limited by the line span with the lowest ampacity — the critical span [10]. These often occur in conjunction with low wind speeds and/or wind parallel to the line [11], where the convective cooling, which is the line's main cooling mechanism [12,13], is low. We argue that in such regimes, existing DTR models may underestimate ampacity, and enhancing model accuracy presents a clear opportunity to improve grid utilisation and robustness.

While DTR implementations can be broadly categorised as either measurement-based (using sag/temperature monitors) or model-based (using a heat balance equation solved with weather and current data [14]), this work focuses on the latter. A review of the state-of-the-art in DTR modelling, particularly concerning the representation of convection, is necessary to frame our contribution.

1.1. Literature review

The foundation of model-based DTR is a heat balance equation where ampacity is determined by balancing internal Joule heating

* Corresponding author at: Jožef Stefan Institute, Jamova cesta 39, Ljubljana, 1000, Ljubljana, Slovenia.
E-mail addresses: nika.mlinaric@ijs.si (N. Mlinarič Hribar), matjaz.depolli@ijs.si (M. Depolli), gregor.kosec@ijs.si (G. Kosec).

https://doi.org/10.1016/j.ecmx.2026.101633
Received 19 June 2025; Received in revised form 22 January 2026; Accepted 26 January 2026
Available online 27 January 2026

Abbreviations

ampacity	ampere capacity
CDF	Cumulative Distribution Function
DTR	Dynamic Thermal Rating
TSO	Transmission System Operator
PDF	Probability Density Function

against external solar heating, radiative cooling, and convection cooling [5,7,8]. Recent studies have advanced the field by addressing overarching model uncertainties [15–17] and by proposing refinements such as additional heat terms for precipitation-driven cooling [18, 19]. However, accounting for wind variability in the convective term remains to be explored.

DTR calculations are usually performed with a temporal resolution of around 1 min to 10 min, and the environmental parameters such as wind speed and direction, ambient temperature and solar radiation are typically averaged over the sampling interval (we will refer to it as averaging window, or short, window). This resolution is sufficient for most of the parameters, as their rate of change is slow. For wind, however, this time scale is quite long, as it is known that both wind speed and direction can vary significantly over a few minutes.

There are no studies of how wind variability affects DTR calculations, however, wind variability itself is a known phenomena. Variability of wind speed is well-researched, especially for strong winds regime [20–22], and it has been shown that the resolution of wind data affects the wind power density assessment [23]. Variability in wind direction is of interest to several fields from wind turbines [24] to air pollutants [25]. It is generally accepted that strong winds have better-defined direction than low winds [7], and similarly, that the variability in wind direction increases with a decrease in speed [26,27]. A study of air pollutants spread [25] performed at low wind speeds found that standard deviation of wind direction within 1 min to 10 min windows was up to 15°–75°, depending on the environment, which is considerable.

This brings us back to averaging. Wind speed and direction are usually measured separately [28], however, wind is a vector quantity. It can be averaged as a vector, or each of the parameters can be averaged separately, as scalars. In applications considering strong winds, such as wind measurement in marine buoys [29,30], or synoptic scales, such as weather forecasts [28], both averaging methods usually give similar results. In the context of critical spans, however, we are mostly interested in low-winds regime, and we will see that the two averaging methods can give significantly different results. As the relationship between wind velocity and heat loss due to convective cooling is highly non-linear, we expect the process of averaging to impact the DTR results.

1.2. Contribution and paper organisation

The aim of this study is to leverage the available high-temporal-resolution wind measurements from an in-service transmission line and perform a first exploratory study on how wind variability and wind averaging, a standard procedure in DTR, affect the DTR calculations. We will show that the effect is significant and that it depends on both wind variability and the choice of the averaging method. This is especially true in the case where the wind is parallel to the line, where taking into account wind variability increases the ampacity. As this often occurs in the critical span, understanding it and accounting for it in DTR would result in increased capacity of the whole line, which is of practical interest to TSOs. On the other hand, averaging can also lead to overestimated ampacity, as we will see in the case with perpendicular wind.

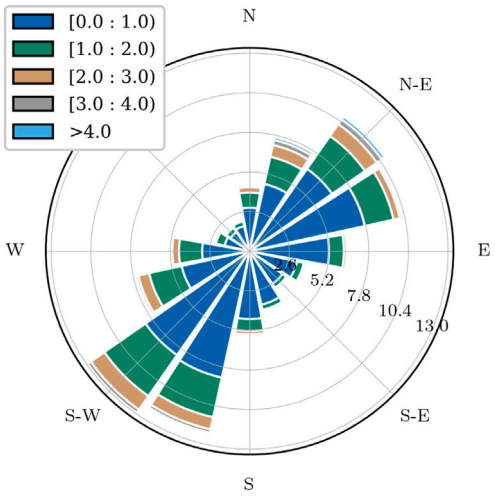

Fig. 1. Wind rose of the 1-second measurements.

The rest of the paper is structured as follows: First, we look at the wind measurements for an in-service transmission line in Slovenia and discuss different averaging methods in 2. We introduce a measure for describing the variability in wind speed and direction in 2.2. We analyse at how wind averaging impacts ampacity calculations in 3. We look at the effect's angular dependency address two limit cases, with the wind parallel and perpendicular to the line in 3.4 and 3.5. We sum up the findings in 4, where we also present the opportunities for future work.

2. Wind data in realistic conditions

2.1. Acquisition and averaging

For the purposes of this study, Slovenian TSO ELES provided wind data with a temporal resolution of 1 s, measured with *WXT 536* ultrasonic wind sensor located on 220 kV Podlog-Obersielach AlFe 490/65 mm^2 line. The sensor's range for wind speed is 0 to 60 $m\,s^{-1}$ with resolution of 0.1 $m\,s^{-1}$ and wind angle resolution is 1°. Both quantities are measured with accuracy of 3 at 10 $m\,s^{-1}$. The sensor's sampling frequency is 4 Hz, and each 1-second measurement is a 3-second running average, in accordance with wind gusts measurement in [28]. The data covers two separate periods: from the 1st to the 30th of April and from the 1st of August to the 30th of September 2024. These were the only periods when the high-resolution measurements were available, as such high resolution is not typical in DTR. The data contained less than 0.02% of missing or invalid measurements, which were dropped from the DTR calculations. The data has not been treated otherwise.

Fig. 1 shows the wind rose of the data. The observed speeds are relatively low with the majority of measurements under 2 $m\,s^{-1}$. The maximum measured speed is 12.1 $m\,s^{-1}$. The angular distribution of the wind measurements shows two predominant directions: one from the east-northeast (peaking around 55°) and the other from the south-southwest (around 210°), with the highest speeds predominantly occurring at these angles. A look at the satellite image of the site in Fig. 2 reveals that the observed strong directional dependence is likely the consequence of the topographic features.

Using a 1 s time resolution is not practical for most DTR applications. In the case of measurement-based DTR, the primary limitation is often the required data communication bandwidth. On the other hand, the temporal resolution of numerical weather prediction is constrained by both the simulation time step and the underlying physics model. Therefore, DTR systems typically rely on averaged values over a time interval with a predefined length - a window, which is generally

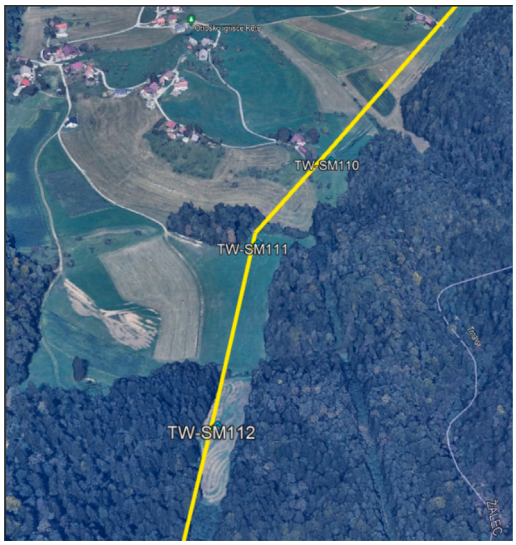

Fig. 2. Satellite image of the considered site. DTR calculations will be performed on the span between pylons SM111 and SM112.

between 1 min and 10 min. We experimented with different lengths, and observed similar qualitative effects on ampacity, with magnitude of these effects varying. In this paper we omit the analysis of window length for brevity, and use 5-minute averaging window throughout, since such a window is also used by the TSO in practice for the line in question.

There are two fundamentally different averaging approaches in use [28,29,31]. The first is vector averaging, where wind vectors are treated as geometric entities, and the second is hybrid approach, where each component of the wind velocity is averaged separately: the wind magnitude is averaged as a scalar value, and the average angle is determined using vector averaging. For the observed location, the TSO uses vector averaging, however, averaging itself is often not discussed at all when talking about DTR, so we assume TSOs often take the default sensor output, and do not concern themselves with the averaging method used by the sensor. In this paper, we will take a look at both approaches.

Mathematically, vector average $\overline{\mathbf{v}_v}\,(\overline{v_v}, \overline{\alpha_v})$ reads as

$$\overline{\mathbf{v}_v} = \frac{1}{n}\sum_{1}^{n}\mathbf{v} \tag{1}$$

and hybrid average $\overline{\mathbf{v}_h}\,(\overline{v_h}, \overline{\alpha_h})$ as

$$\overline{\mathbf{v}_h} = \left(\frac{1}{n}\sum_{1}^{n} v, \overline{\alpha_v}\right) \tag{2}$$

with n standing for number of samples in one window and $\overline{\alpha_v}$ for the angle obtained through vector averaging. Generally, if the application only depends on wind speed, scalar average is more suitable, and if direction is also important, like in particle transport, vector averaging performs better [31].

In DTR, both speed and direction are important, and as we will see in Section 3, where the mathematical model for convective heat exchange with the surrounding air is discussed, the relationship between wind velocity and heat flux is highly non-linear. As a result, there is no one obvious averaging method choice, and the averaging method has a significant impact on DTR.

For instance, consider an extreme case where during half of the window, significant wind blows parallel to the line from one side, and during the other half, it blows from the opposite direction with equal magnitude. The wind cooling effect would be the same as if it had been consistently blowing from one direction only. However, in such a scenario, vector averaging would yield net wind of zero (therefore underestimating the cooling), and in hybrid averaging, the wind angle would at worst not be defined and at best be at 90° relative to the line. We will see in Section 3 that convective cooling depends on the relative angle of the wind, and that it is most efficient when the wind is perpendicular to the line, which means hybrid averaging would overestimate the cooling in this case.

Let us take a look at both averaging methods in the context of the observed data. Fig. 3 presents two examples of wind measurements taken over 5 min windows. Example A (April 10th, from 14:50 to 14:55) corresponds to above-average wind speeds, approximately $5\,\mathrm{m\,s^{-1}}$, where the wind direction remains relatively consistent throughout the window. In contrast, wind in example B (April 4th, from 13:50 to 13:55) has lower speeds, around $1\,\mathrm{m\,s^{-1}}$, and wind direction varies significantly, covering nearly the entire range of possible directions. We see that in example A, both averaging methods yield similar results, whereas in example B, there is a considerable difference between the two average wind speeds, with the vector-averaged speed being much lower than the hybrid-averaged one.

2.2. Wind variability within the averaging window

In the previous section we established the ground for introducing the concept of the wind variability [32,33]. In general, wind variability is discussed across different temporal scales, ranging from minutes to seasons. In the context of this paper, wind variability refers specifically to fluctuations in wind speed and direction over one window, i.e., over short time scales.

We define a variability metric ξ as

$$\xi_X = X_{p,\mathrm{hi}} - X_{p,\mathrm{lo}} \tag{3}$$

where X is either wind speed or direction, and $X_{p,lo}$ and $X_{p,hi}$ are the lower and upper limits for which cumulative distribution function CDF(X) equals $\frac{1-p}{2}$ and $1-\frac{1-p}{2}$, respectively. For the variability in speed, ξ_v, the quantity X is simply the measured speed, whereas for the direction, X is the direction subtracted by its average in each window and observed on the interval from −180° to 180° to account for the scale discontinuity, $\xi_\alpha := \xi_{\alpha-\overline{\alpha}}$. The definition is presented schematically in Fig. 4. We take $p = 0.68$, which means the proposed metric ξ is equivalent to standard deviation if X is normally distributed. I.e. $\xi = 2\sigma$, where

$$\sigma_x = \sqrt{\frac{\sum_{i=1}^{n}(x_i - \overline{x})^2}{n}} \tag{4}$$

with x_i representing the ith measurement, $\overline{x}$ is the mean of all the measurements, and n is the number of measurements. Generally however, the speed and direction are not normally distributed. Especially with the direction, we have observed a plethora of different shapes, including multi-modal, which makes defining a variability measure challenging and poses an opportunity for further studies. In a multi-modal case, we believe the variability metric ξ_X holds more information than the standard deviation, as it takes the lower and upper limits of X into account, which hold information about the asymmetry of the distribution. Fig. 4 shows the probability distribution functions (PDFs) for wind direction for examples A and B, along with the appropriate upper and lower limits of variability metric.

Fig. 5 shows the variability in the observed data for all of the 5-minute windows. We see that for wind speed, variability is generally between $0\,\mathrm{m\,s^{-1}}$ and $3\,\mathrm{m\,s^{-1}}$, which is considerable given the observed low wind speeds. The PDF for wind direction variability has a peak at around 40°, followed by a plateau and a cut-off at around 200°. Again, this variability is considerable.

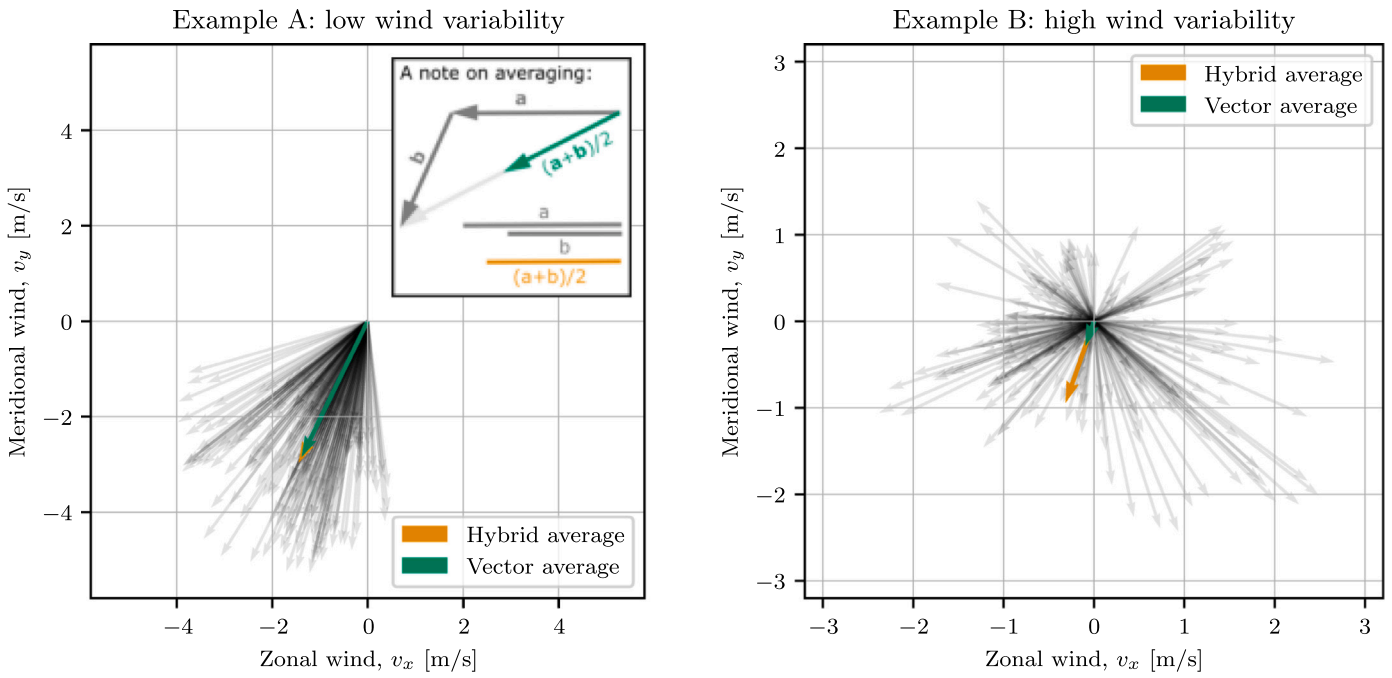

Fig. 3. Vector plot of 1 s wind measurements and average values within one 5 min window. Example A has higher wind speeds and relatively constant wind direction and example B has lower wind speed and significant variations in wind direction.

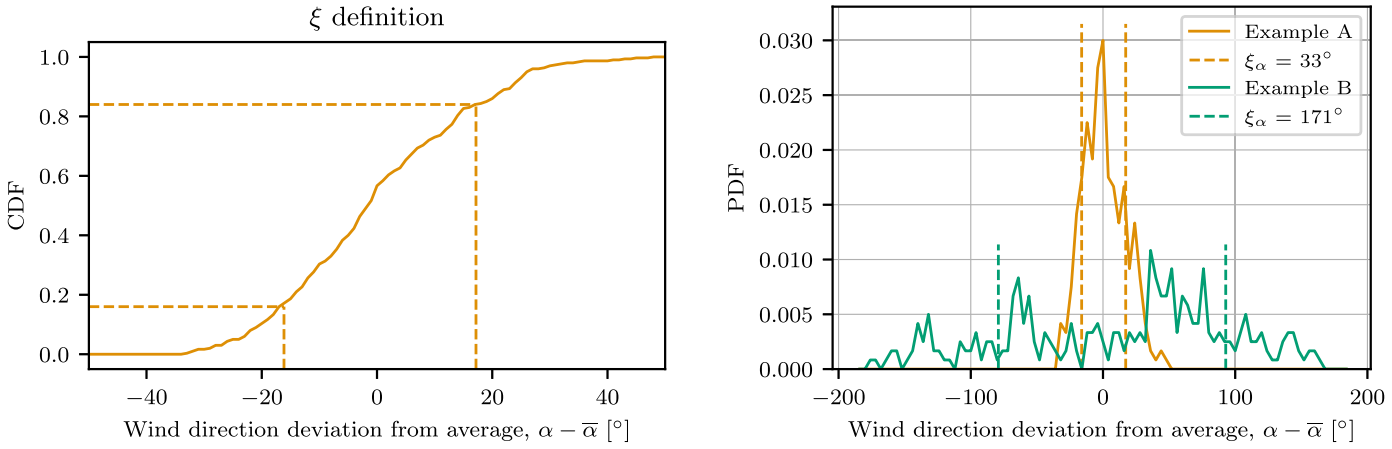

Fig. 4. The schematic representation of the ξ definition (left) and wind direction probability density functions (PDFs) for examples A and B along with the wind direction variability metric ξ_α's upper and lower limits (right). The wind directions are shown relative to the average wind direction in each window. Note that the calculation of the average angle is weighted by wind speed, so the average angle might not seem intuitive, especially for example B.

3. Effect of wind averaging on ampacity calculations

3.1. DTR model

Now, let us take a look at how wind variability affects ampacity calculations. The calculations in this paper are performed according to CIGRE guide [7]. The ampacity is given by

$$I_{th} = \sqrt{-\frac{Q_s(T_{max}) + Q_r(T_{max}) + Q_c(T_{max})}{k_s R_{dc}(T_{max})}} \text{[A]} \tag{5}$$

where k_s is the skin effect factor, R_{dc} is the direct current resistance and T_{max} is the maximum allowed conductor temperature. In Slovenia, $T_{max} = 80\,°\text{C}$, and this value is used in the calculations. Q_s, Q_r and Q_c are solar heating, radiative cooling and convective cooling, respectively. Solar heating given by

$$Q_s = 2\alpha I_s r_2 \quad [\text{W m}^{-1}] \tag{6}$$

with α being conductor surface absorptivity, characteristic of the line, and I_s is the global radiation intensity, which can be either measured or estimated from geographical location. r_2 is the line radius. Radiative cooling is given by

$$Q_r = -2\pi r_2 \sigma_B \epsilon \left[T_s^4 - T_a^4\right] \quad [\text{W m}^{-1}] \tag{7}$$

with σ_B the Stefan–Boltzmann constant, ϵ is conductor surface emissivity, characteristic of the line, T_s is the skin temperature of the line and T_a is the ambient (air) temperature, which is usually measured.

The last cooling contribution is convective cooling, which is the main cooling contribution and the only contribution featuring wind. It is given by

$$Q_c = -\pi \lambda_f (T_s - T_a)\text{Nu} \quad [\text{W m}^{-1}] \tag{8}$$

where λ_f is thermal conductivity of air at film temperature, $T_f = (T_s + T_a)/2$, given in CIGRE. Nu is Nusselt number. In the case of zero wind, convective cooling is present in the form of natural convection,

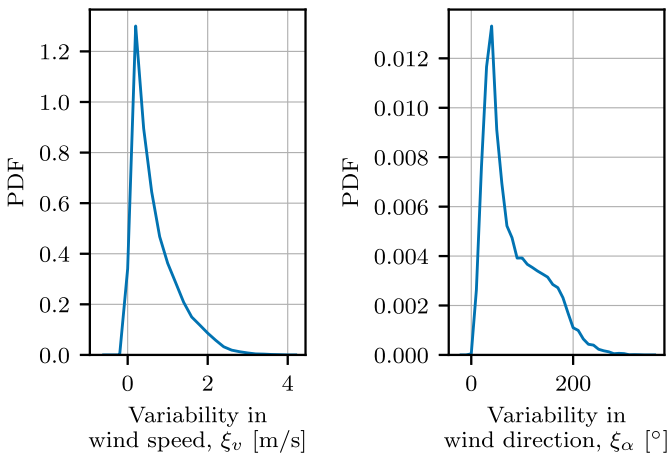

Fig. 5. Probability density functions (PDFs) for variability in wind speed and direction for the observed data.

and the Nusselt number is given by

$$\mathrm{Nu}_{\text{natural convection}} = A(\mathrm{GrPr})^m \tag{9}$$

where Gr is Grashof number and Pr is Prandtl number and A and m are scalar parameters that are given in tables for different values of GrPr.

In case of strong wind, the Nusselt number for the perpendicular flow is given by

$$\mathrm{Nu}_{90} = B\mathrm{Re}^n \tag{10}$$

with Reynolds number $\mathrm{Re} = 2r_2 v/\nu_f$; r_2 is the radius of the conductor, v is wind speed, and ν_f is kinematic viscosity of air at film temperature. Parameters B and n are given in tables and depend on both Re and the roughness of the conductor surface. The following corrections are given for the wind direction relative to the conductor axis α_{rel}

$$\begin{aligned}\mathrm{Nu} &= \mathrm{Nu}_{90}(0.42 + 0.68(\sin(\alpha_{rel}))^{1.08}),\ \alpha_{rel} \le 24°\\ \mathrm{Nu} &= \mathrm{Nu}_{90}(0.42 + 0.58(\sin(\alpha_{rel}))^{0.90}),\ \alpha_{rel} > 24°.\end{aligned} \tag{11}$$

In practice, the transition between the natural and forced convection occurs at around $0.5\,\mathrm{m\,s^{-1}}$, and for low wind speeds, CIGRE recommends calculating both forced and natural convection, then using the higher of the two values.

CIGRE notes that the Nusselt number relations can be considered as the local performance of the conductor in constant laminar wind, and that the Nusselt number increases with the intensity and scale of the turbulence, but it does not provide any relations, and states that the turbulence assessment is very complicated for real-life installations. In the context of this study and the high temporal resolution of the observed data, we will use these relations for short time scales, in an effort to make the first exploratory step to high-resolution DTR. However, further studies are needed to explore the validity of the relations over different (shorter) time scales, and variable wind. We see this as a potential for future work.

To isolate the effect of wind measurements, which are the core of the presented study, all of the other weather parameters are set to constant values for further analysis. To set realistic conditions that would be of interest to TSOs, solar radiation and temperature are set to match a typical sunny day, with an average temperature for timespan between April (the coldest of the observed months) and August (the warmest of the observed months) for the observed location. I.e. $I_s = 900\,\mathrm{W\,m^{-1}}$, and $T_a = 15\,°\mathrm{C}$. The observed line span lies between pylons SM111 and SM112 in Fig. 2, which means the line direction at the point of interest is north–south and the prevailing wind directions are neither parallel nor perpendicular.

3.2. Effects on the in-service line

With the model defined, we can take a look at some real-life data. First, let us take a look at two illustrative examples of how the combination of wind variability and averaging method affects the results. Fig. 6 shows the wind speed and direction timelines of examples A and B along with the calculated ampacity. The high-resolution calculations are performed with 1 s wind measurements, and the average of these calculations $\overline{I_{th}(w)}$ will serve as the benchmark for comparison. It will be compared to ampacities calculated on 5 min averaged wind measurements, $I_{th}(\overline{w})$, for both averaging methods.

In example A, the three ampacities are within 45 A (3), with both ampacities calculated on the averaged data being just above the $\overline{I_{th}(w)}$. The observed small difference in results is expected, as we have seen in Fig. 3 that with well-defined wind direction and low ξ_α, the scalar and vector average of the wind speed are close together (also within 4), and speed averaged in either way is representative of the whole window. Example A clearly represents a favourable situation for using the averages in DTR calculations.

On the other hand, in example B, the hybrid-averaged data ampacity is around 140 A (11) lower than $\overline{I_{th}(w)}$, and vector-averaged data ampacity is around 290 A (23) lower than $\overline{I_{th}(w)}$. Both differences are substantial. There are two effects that contribute to the differences. First, vector-averaged speed is significantly lower than the scalar-averaged speed (almost 80 lower), which is due to large ξ_α. Second, if we look at the relative angle distribution, we see that most values lie above 40°, which is favourable for convective cooling. But the average relative angle is much lower, around 19°. We can understand this if we take a look at Fig. 3 (right), where we see that we get significant wind contributions from the east- and westward directions, however, the average angle gives us wind from the north-northeast. With the observed line span in the north–south direction, the averaging results in a lower relative angle which creates a less favourable cooling scenario, and this is true for both averaging methods, as wind direction is the same by definition.

Examples A and B were chosen from the best- and worst-case ends of the spectrum. Let us now examine the whole dataset to assess the overall effect. Fig. 7 shows the distribution of relative differences of ampacities calculated on averaged data vs high-resolution data for both averaging methods for the whole dataset. With vector averaging, ampacity was higher than $\overline{I_{th}(w)}$ around 20 of the time, and the highest difference was quite limited with the amount of time exceeding 5 difference being negligible. The majority of time, ampacity computed on averaged data was lower than $\overline{I_{th}(w)}$. The differences amounted to being higher than 10 in 13 of the time and higher than 20 in 3 of the time.

With hybrid averaging, the relative differences distribution is more symmetric, and underestimates the ampacity 45 of the time. For 4 of the time it underestimates $\overline{I_{th}(w)}$ for more than 10 and for less than around 0.5 % of the time it underestimates $\overline{I_{th}(w)}$ for more than 20. On the other hand, around 2 of the time ampacity overestimates $\overline{I_{th}(w)}$ for more than 10.

3.3. Angular dependency

We have seen in example B that relative angle plays an important role, so let us take a look at how ampacity difference changes with the average relative angle. Fig. 8 shows the distribution of relative ampacity differences for 5 min windows for both averaging methods, broken down by average relative angles. With vector averaging, the distributions appear heavily asymmetric, with $\overline{I_{th}(w)}$ being underestimated the majority of time. The tails are the longest for small relative angles, while with the increasing relative angle, the amount of underestimated ampacities decreases and the distributions become narrower, with the peaks moving towards the right. At small relative angles under 15°, ampacity based on averaged data underestimates the $\overline{I_{th}(w)}$ for more

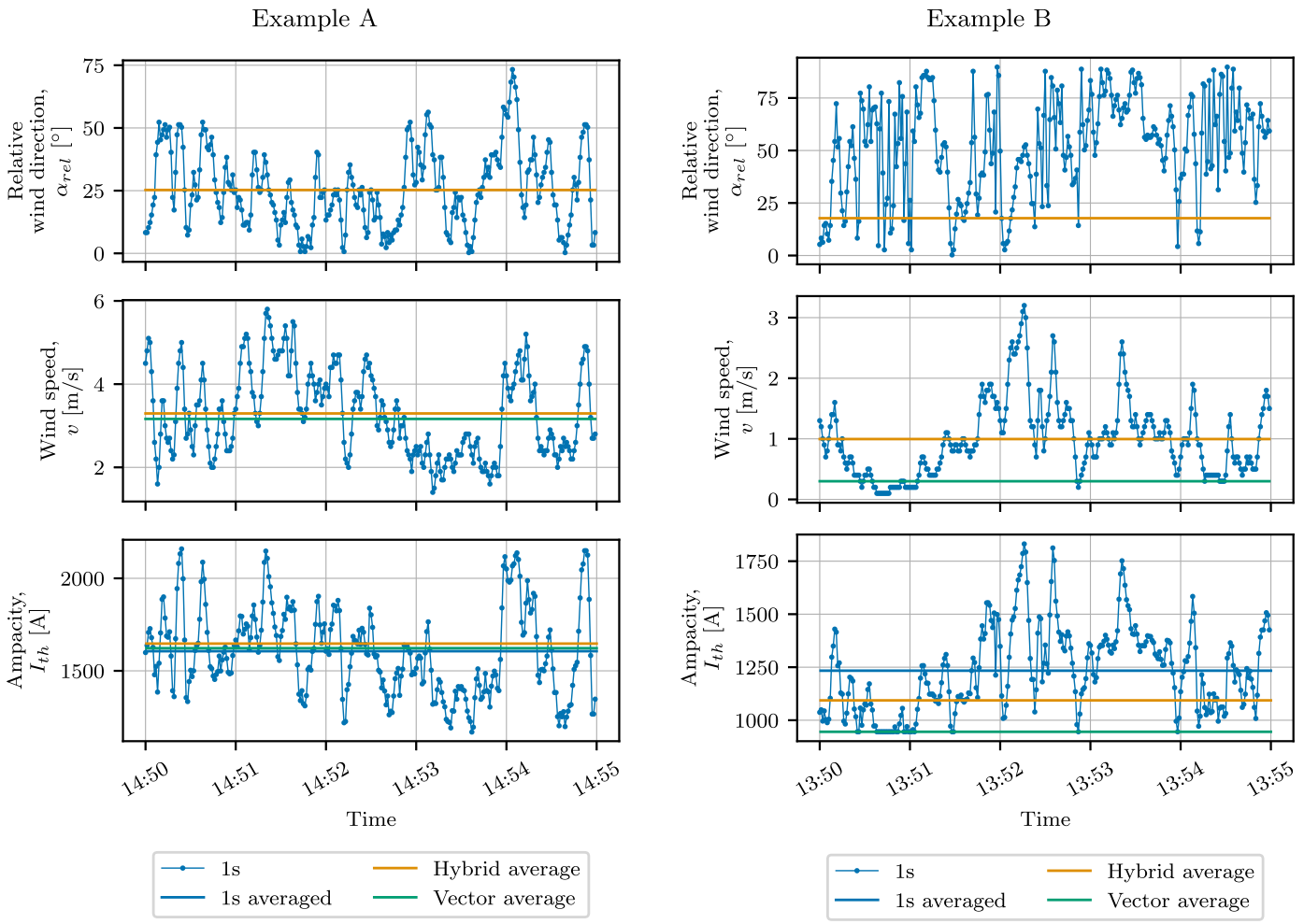

Fig. 6. Relative wind direction and wind speed measurements and ampacity calculations for high-resolution measurements and both averaging methods. Example A has higher wind speeds and low wind direction variability ξ_α and example B has lower wind speeds and high wind direction variability ξ_α. Note that by definition, the average angle is the same in vector and hybrid averaging used in this study.

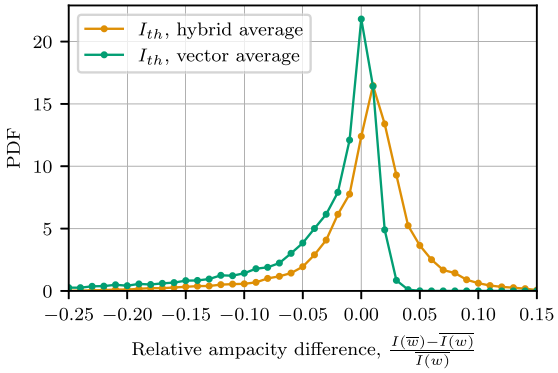

Fig. 7. Probability density function (PDF) of relative differences between ampacity calculated on averaged data $I_{th}(\overline{w})$ and the averaged high-resolution data ampacity, $\overline{I_{th}(w)}$.

than 10 around 37 of the time, and for more than 20 for more than 14 of the time. At close-to-perpendicular wind where the highest percentage of time overestimates $\overline{I_{th}(w)}$, the amount of time that ampacity based on averaged data overestimates $\overline{I_{th}(w)}$ for more than 4 are negligible.

With hybrid averaging, the distributions again become more symmetric. At lower relative angles, longer tails in the negative direction can be observed — average-based ampacity underestimates $\overline{I_{th}(w)}$. With the increase in angle, the tails shift towards the right, with $\overline{I_{th}(w)}$ being overestimated a significant proportion of time. Observing the numbers, the underestimated $\overline{I_{th}(w)}$ has smaller absolute relative differences at close-to-parallel wind than with vector averaging. A bit over 32 of the time $\overline{I_{th}(w)}$ is underestimated for more than 10, and only around 3 of the time it is by 20 or more. On the other hand, around 8 of the time $\overline{I_{th}(w)}$ is overestimated for more than 10 at the close-to-perpendicular wind. Table 1 shows the more detailed breakdown of the relative ampacity difference for all of the relative angles, for both averaging methods.

Intuitively, the observed shift from underestimating $\overline{I_{th}(w)}$ to overestimating it with the increase in the angle is expected. Consider the case with parallel wind. The average angle is 0° and according to Eq. (11), the Nusselt number has a local minimum, so any variability in wind direction increases the cooling. Therefore with averaging, we are looking at the worst-case scenario, so we expect that $\overline{I_{th}(w)}$ will be higher than that. On the other hand, with average wind at 90°, this is the local maximum of the Nusselt number, and the averaging results in the best scenario. Any variability in wind direction decreases the cooling. For the relative angles in between, the variability in wind direction means there are times with better and times with worse cooling, with the effect partially cancelling itself out, making the tails in the distribution of differences less pronounced. Note that the transition between the two extremes is not linear. This can be seen from as

Table 1
The amount of time the relative ampacity difference $\frac{I_{th}(\overline{w})-\overline{I_{th}(w)}}{\overline{I_{th}(w)}}$ is less than or greater than the stated value. The results are given in % of time.

α_{rel}	Vector averaging					Hybrid averaging				
	≤ −0.2	≤ −0.1	≤ 0	> 0.05	> 0.1	≤ −0.2	≤ −0.1	≤ 0	> 0.05	> 0.1
0°–15°	14.5	37.0	97.8	0	0	3.1	32.2	97.7	0	0
15°–30°	4.6	17.0	83.0	0	0	0	3.3	68.8	0	0
30°–45°	1.2	6.9	60.1	0	0	0	0	31.9	1.0	0
45°–60°	1.0	5.8	53.3	0	0	0	0	19.3	9.2	0.5
60°–75°	0.9	6.8	55.4	0	0	0	0	14.5	24.5	3.8
75°–90°	0.8	7.1	57.9	0	0	0	0	11.8	34.1	7.9

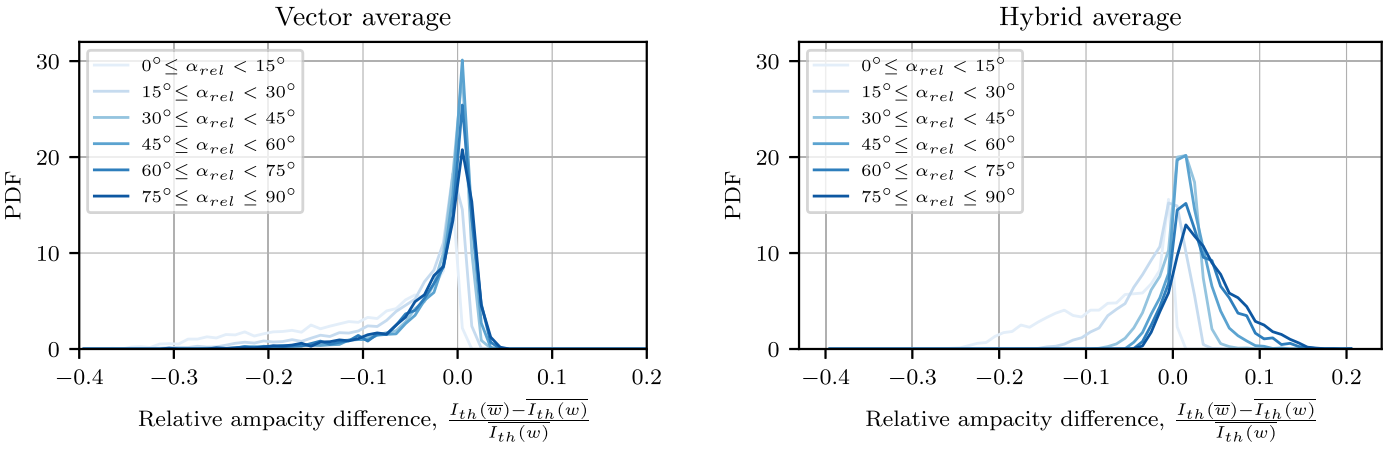

Fig. 8. Probability density function (PDF) of relative differences between ampacity calculated on averaged data $I_{th}(\overline{w})$ and the averaged high-resolution data ampacity, $\overline{I_{th}(w)}$ for both averaging methods, with a breakdown for different relative wind angles α_{rel}.

Eq. (11), which includes sine dependence, as well as a step-change in parameters.

Establishing that relative angle is an important factor, we will discuss two limit cases where the relative angle is 0° and 90°, respectively.

3.4. Parallel wind and critical spans

Let us first take a look at the case with the parallel wind, which is where the convective cooling is the least effective. Due to sine dependency in Eq. (11), this is the limit case where the Nusselt number and consequently convection are the most sensitive to the changes in relative angle. In practice, the critical spans are often the spans with parallel wind. Therefore, the accuracy of calculated ampacities could have a significant effect on line operation in this regime.

As the span of the available data for analysis is relatively short (3 months), and skewed with the uneven wind direction distribution, we must augment the data to support further analysis. We start from the static property of the ampacity. Since ampacity is defined for static conditions, it can be computed for each time window in isolation and neighbouring time windows do not impact it. To control the wind angle, we can rotate it uniformly without affecting its variability. Therefore, we will split the data into 5 min windows and independently rotate the wind within each window so that the average relative angle of the rotated data is 0°.

We then calculate the ampacities for the whole dataset. Fig. 9 shows the distribution of relative ampacity differences for both averaging methods. As mentioned above, convective cooling is the least effective at $\alpha_{rel} = 0°$, so any variability in wind direction increases the cooling. This explains why ampacities computed on averaged data underestimate $\overline{I_{th}(w)}$. The maximum observed underestimation was an astounding 46%, obtained with vector averaging. The overall shapes of PDFs are similar for both averaging methods, with the distribution for vector averaging having longer tails. Looking at the shape of the distribution, it is immediately obvious that it is different than in Fig. 7,

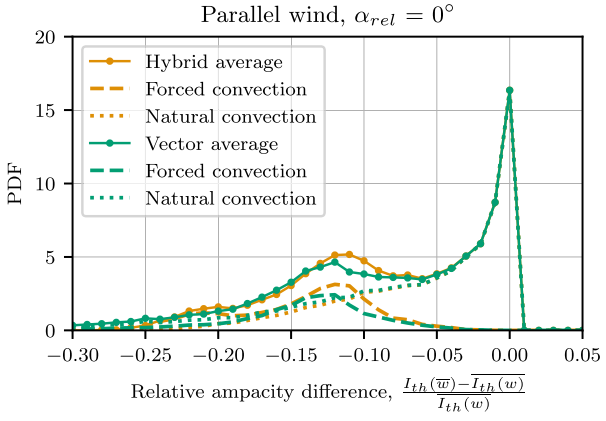

Fig. 9. Probability density function (PDF) of relative differences between ampacity calculated on averaged data $I_{th}(\overline{w})$ and the averaged high-resolution data ampacity, $\overline{I_{th}(w)}$ for $\alpha_{rel} = 0°$. Plot shows calculations with hybrid and vector averaging and the breakdown in forced and natural convection regimes. The averaged-data ampacity underestimates the 'true' ampacity for up to 30% - this is a potential for line capacity increase.

which had one prominent peak. Here we get two peaks, the first and more prominent at 0, and the second, less prominent at around −0.12. The multi modal shape suggests there may be more than one underlying mechanism, and we can see that this is indeed the case if we segment the plot into the natural and forced convection.

As mentioned in Section 3, CIGRE differentiates between forced and natural convection regimes. For low wind speeds, both natural and forced convection are calculated, and the higher of the values is taken for the convection contribution. This model does not fully represent

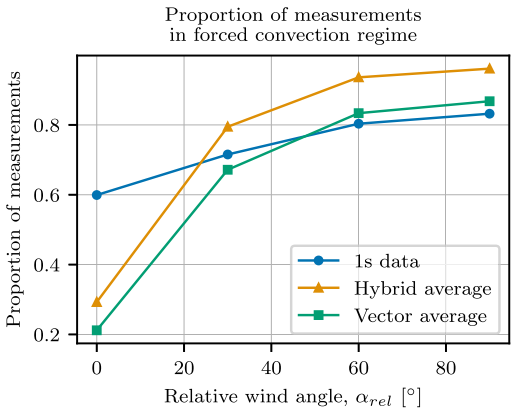

Fig. 10. Proportion of cases that fall into forced convection regime depending on the relative direction of the wind for 1 s data and both averaging methods.

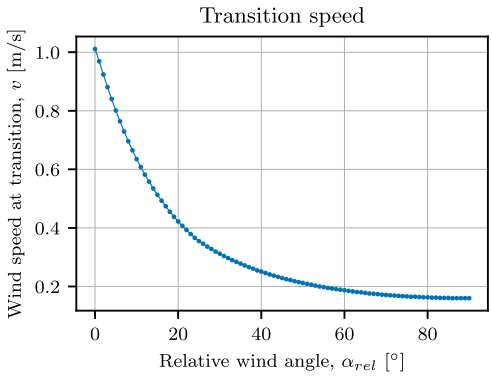

Fig. 11. The speed at which transition between forced and natural convection occurs for $T_s = 80\,°C$ and $T_a = 15\,°C$, depending on the relative wind angle.

the reality, as airflow in practice is driven by a combination of forced movement from wind and the natural rise of hot air. However the model explains the multi-modal shape of the graph. We can clearly see that the spike at around 0 is due to natural convection, and the distribution for the forced-convection regime has a peak between −0.2 and −0.1. Note that classification into regimes is done based 5-minute averaged data. In practice, for any 5 min window classified as one convection regime, some of the 1 s data within that window may actually fall in the other regime.

Another thing that draws our attention is that a substantial proportion of samples lies within the natural convection regime — more than in the forced convection. Based on our previous experience with DTR for this location, this is somewhat unexpected. We can explain it with Fig. 10, which shows the proportion of samples with dominant forced convection regime for 1 s data and 5 min averaged data, as a function of the relative angle. We notice that generally, the proportion rises with the average angle. The proportion for the average data falls drastically at $\overline{\alpha_{rel}} = 0°$, and it is much lower for averaged data than for 1 s data.

This can be explained with Fig. 11, which shows the speed at which the transition between natural and forced convection occurs (we will refer to it as transition speed) at the selected conditions, i.e. the selected constant air temperature and maximum conductor temperature. The transition speed decreases with the angle, and has the steepest slope around 0°, so any variability in wind direction can cause the 1 s data sample to fall into a different regime than the averaged data sample. It can also be clearly seen from Fig. 10 that for all angles, more data falls into the natural convection regime with vector averaging, compared to hybrid averaging. This is because for windows with large variability in the direction, the vector averaging dampens the speed.

Fig. 9 established that there is a difference between ampacity computed on averaged data versus computed as $\overline{I_{th}(w)}$. Let us take a look at how this difference depends on wind direction variability and wind speed, which is shown in Fig. 12. Note that the colour scale is truncated for clarity. We can see that the plots for vector and hybrid averaging have similar shapes. For both types of averaging, the absolute minimum relative ampacity differences are obtained at low wind speeds and low variabilities in wind direction. The relative difference becomes larger (in the negative direction) with the increase of both parameters.

Fig. 13 shows the cross-sections of the scatter plot for different speed intervals. We can see that for all speed ranges, with increasing ξ_α, the ampacity difference first gets more negative, and then reaches a plateau. A plateau is expected, as ampacity is dependent on the relative angle, so there is a point when the increase in direction variability does not introduce any new relative angles. The location of the plateau depends on the parameter p in our definition of variability in Eq. (3).

As shown in Fig. 10, for velocities exceeding approximately $1\,m\,s^{-1}$, forced convection dominates over natural convection. This is further evident in Fig. 13, where the plots corresponding to the forced convection regime exhibit only minor differences.

The observed dependency could serve as a measure for evaluation of the discrepancy in the ampacity of the averaged data compared to the $\overline{I_{th}(w)}$, provided that the information about wind variability inside the window is available. This could potentially be of great interest in practice, as it effectively means that the majority of time when operating in parallel wind, the ampacity is underestimated. In the observed data, if wind variability was accounted for properly, the ampacity estimate could be raised considerably. However, further analysis and a better model are needed before it can be adopted by TSOs.

3.5. Perpendicular wind

Let us now consider the opposite limit case, where the relative angle is 90° and the convective cooling is the most effective. Fig. 14 shows the relative ampacity difference distribution for both averaging methods. Convective cooling at 90° is the most effective, so any variability in wind angle lowers the convective cooling. This is why averaging overpredicts the ampacity for a considerable amount of time, which is especially true for hybrid averaging, where the scalar average of the speed does not dampen the amplitude with increased variability. The overall maximum observed overestimation in the data was 28%. On the other hand, vector averaging does dampen the amplitude, which is why in this case, ampacity is underpredicted for a considerable amount of time. Note that the proportion of the natural convection regime is much lower than with parallel wind, which is in accordance with the lower transition speed from Fig. 10.

Next, Fig. 15 shows how relative ampacity difference depends on wind speed and ξ_α. For the hybrid average, the shape of the graph is reversed in comparison with the parallel wind case. The minimum differences are again obtained at low values of both parameters and then increase with the increase in either parameter. The sign of the relative difference is different than in the parallel wind case, as is expected, and the maximum amplitude is smaller, which is also expected, because of the sine dependency on the relative angle in Nusselt number calculations in Eq. (11). We can see this effect also in Fig. 16, where we get the nearly linear increase of the relative difference followed by a plateau, mirroring the case with parallel wind.

For vector averaging, the scatter plots are qualitatively different. In parallel wind case, we have two effects that caused the ampacity on averaged data to be lower than $\overline{I_{th}(w)}$, namely vector averaging which dampens the wind amplitude, and the ineffectiveness of cooling at $\alpha_{rel} = 0°$. In perpendicular wind case, the two effects work in opposite directions: the dampening of amplitude still lowers ampacity, but at $\alpha_{rel} = 90°$, cooling by convection is the most effective, thus raising

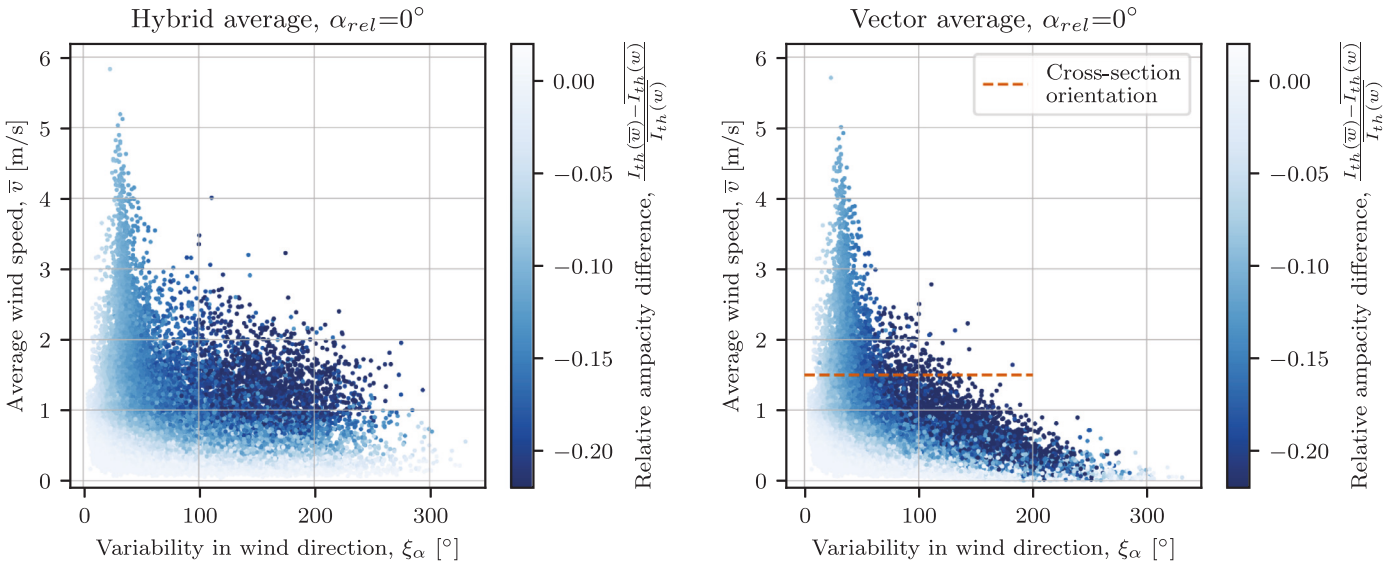

Fig. 12. Relative ampacity differences in parallel wind case as a function of variability in wind direction ξ_α and average wind speed $\overline{v}$ for hybrid and vector averaging. Note that the scale is truncated for clarity. With the increase in $\xi\alpha$ and $\overline{v}$, the averaged data results in underestimated ampacity.

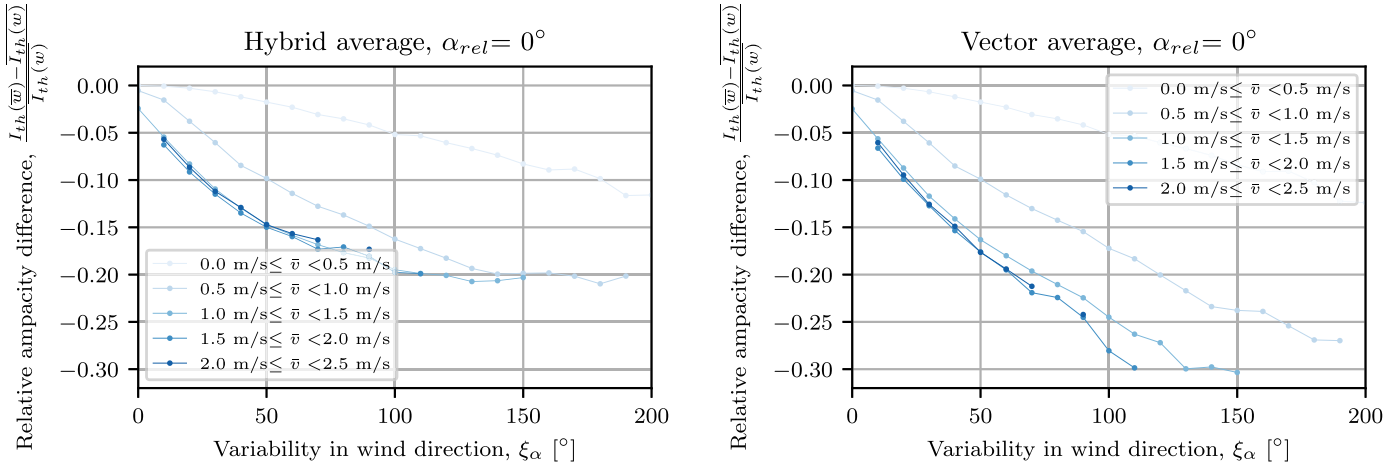

Fig. 13. The cross-section plots showing relative ampacity difference in parallel wind case as a function of wind direction variability ξ_α for hybrid and vector averaging, with a breakdown in wind speed intervals. We can see a clear functional dependency, which means knowing wind speed and wind direction variability would allow us to estimate the ampacity difference.

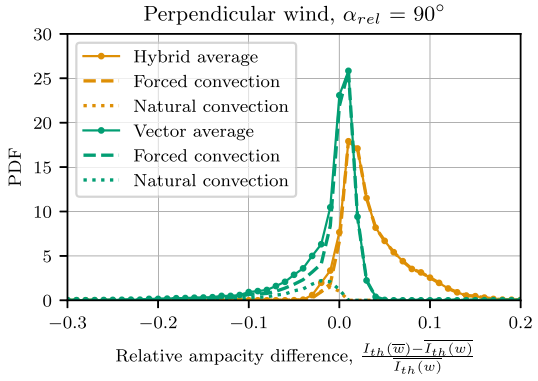

Fig. 14. Probability density function (PDF) of relative differences between ampacity calculated on averaged data $I_{th}(\overline{w})$ and the averaged high-resolution data ampacity, $\overline{I_{th}(w)}$ for α_{rel} = 90°. Plot shows calculations with hybrid and vector averaging and the breakdown in forced and natural convection regimes. With hybrid-averaged data, ampacity can be overestimated by more than 10%, potentially leading to unsafe operation.

ampacity. The different functional shapes of the two methods can also be seen if we look at the cross-sections in Fig. 16. For vector averaging, a plateau appears at low ξ_α, where the two effects cancel each other out, and starting from around ξ_α = 100°, the vector averaged speed dampening becomes dominant, resulting in the similar (near-linear) decrease as in the parallel wind case.

In light of these qualitatively different results, the choice of the averaging method becomes even more important in perpendicular wind case. While hybrid averaging seemed like a better choice in the previous sections, that is not the case here, as overpredicting ampacity could lead to unsafe operation.

4. Conclusion

In this paper, we performed the DTR calculations with the standard 5-minute averaged data, and compared them with DTR calculations with uniquely available high-resolution (1 s) wind measurements for an in-service transmission line in Slovenia. We used two averaging methods, namely vector averaging where wind velocity is averaged as a vector entity, and hybrid average, where the wind direction is averaged with vector averaging, and wind speed is averaged as a scalar.

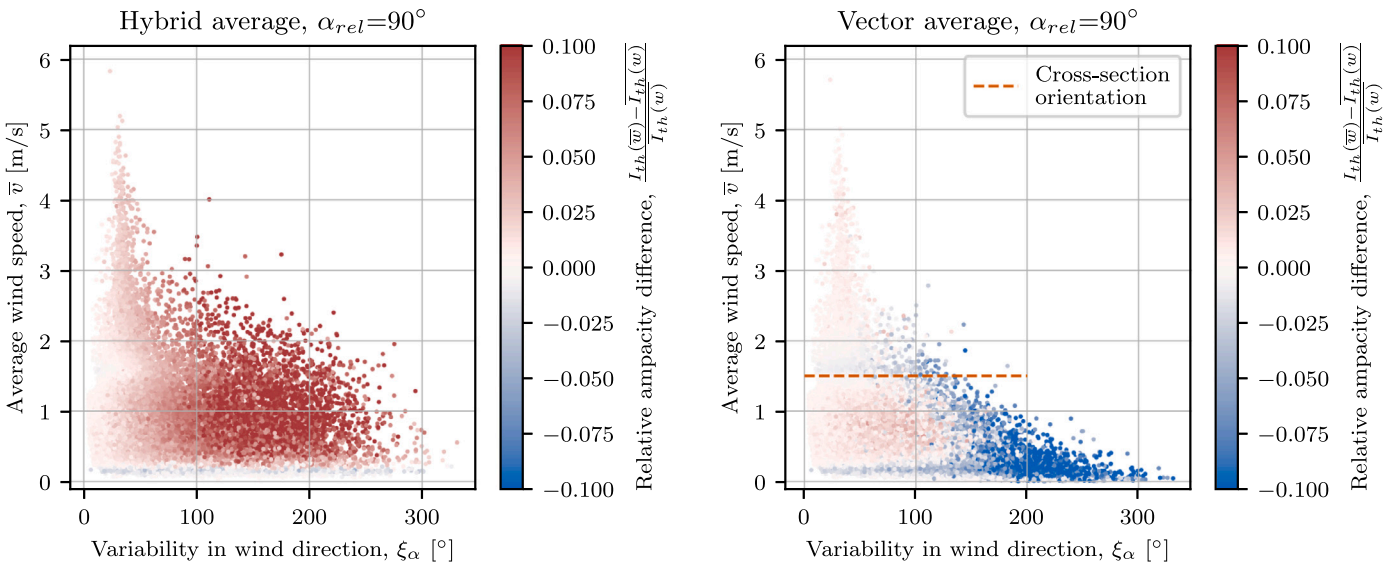

Fig. 15. Relative ampacity differences in perpendicular wind case as a function of variability in wind direction ξ_α and average wind speed $\overline{v}$ for hybrid and vector averaging. With hybrid averaging, there is a large area with overestimated ampacity, while with vector averaging, the plot seems qualitatively different.

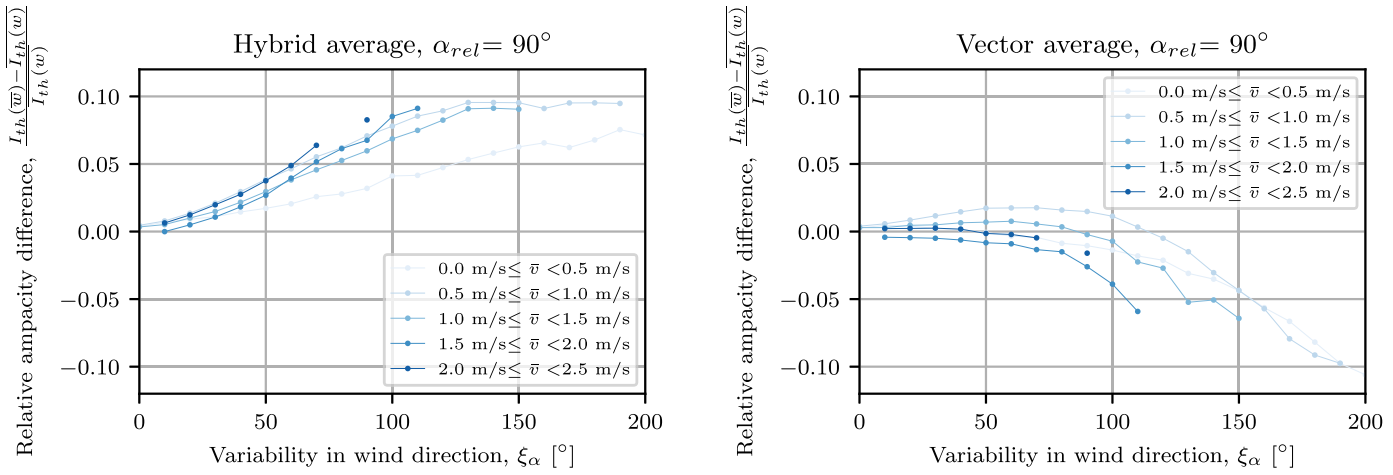

Fig. 16. The cross-section plots showing relative ampacity difference in perpendicular wind case as a function of wind direction variability ξ_α for hybrid and vector averaging, with a breakdown for several wind speed intervals. Again, there is a clear functional dependency, so knowing wind speed and wind direction variability would allow us to estimate the ampacity difference.

We presented a case with low variability in wind direction, where both averaging methods give ampacities similar to the data with higher temporal resolution, and a case with high variability in wind direction where the averaging affects the ampacity significantly. We compared the ampacity differences of the high-resolution data and averaged data for the whole data set. Looking at the 3-month period, averaging has a measurable effect on the DTR results.

We saw that the effect has a strong angular dependency and examined two limit cases, with wind parallel and perpendicular to the line. The case with parallel wind is of special interest to TSOs as critical spans, which limit the ampacity of the whole line, often occur where the wind is parallel to the line. We found that using measurements with higher temporal resolution significantly increases the ampacity for both averaging methods, with the relative potential increase up to 30%. Vector averaging gives lower ampacities than scalar averaging, so TSOs using vector averaging can benefit more from the use of higher temporal resolutions. At the other hand, in the case with perpendicular wind, the use of averaged data can lead to overpredicted ampacities, and the two averaging methods affect the calculations differently.

Furthermore, we found that in both limit cases, the difference between the high-resolution data ampacity and averaged data ampacity can be estimated if the variability in wind direction and the average wind speed are known.

We also observed that for low wind speeds, the CIGRE model itself impacts the ampacity difference distributions due to its handling of the transition between natural and forced convection. Averaging can shift the computational regime from forced convection for 1 s resolution data to natural convection for the averaged data. We believe this could be explored further, and that selection of a different convection model would impact the results of the analysis. The general outcomes, however, should be robust to the selection of models.

This study was a first exploratory step to demonstrate that wind averaging has a significant effect on the ampacity calculations. It used data from a single location, with limited time span, so the ampacity differences found in this study are valid for the characteristic wind on the observed location, and the chosen limit temperature and weather parameters. Further studies with more site diversity and different weather conditions are needed before the findings can be generalised. The present work could also be expanded with a study of the effect of the averaging window length.

It should be noted that a steady-state DTR formulation is applied to high-resolution wind data in order to isolate the effect of wind

averaging, rather than to validate convective heat transfer correlations at second-scale resolution. Applying the CIGRE steady-state model at 1 s resolution approaches the temporal limits of the underlying convection model, in which steady flow without transient effects is assumed. Furthermore, the computed 1 s ampacity values represent theoretical instantaneous steady-state ratings, used here as a diagnostic construct to examine the non-commutativity between averaging and nonlinear convective heat transfer, and are not intended to be interpreted as realistic line capacities.

Future work will address a more comprehensive analysis of wind speed and wind-to-line angle distributions to gain further insight, as well as transient and turbulence-resolving approaches, including CFD-based analyses and model developments that explicitly account for wind variability beyond heuristic treatments such as wind clipping [2].

The main takeaway of this paper is that wind variability paired with the averaging of wind data significantly affects the DTR ampacity calculations, and that the choice of the averaging method is important. In the case of parallel wind, higher resolution data gives higher ampacity, which could be of interest to TSOs in case of limiting spans. However, more data is needed before the findings can be generalised and put into practice. We hope that this exploratory study will open the door for further research in the field.

CRediT authorship contribution statement

Nika Mlinarič Hribar: Writing – review & editing, Writing – original draft, Visualization, Validation, Software, Methodology, Investigation, Formal analysis, Data curation, Conceptualization. **Matjaž Depolli:** Writing – review & editing, Validation, Software, Methodology, Conceptualization. **Gregor Kosec:** Writing – review & editing, Supervision, Software, Resources, Methodology, Funding acquisition, Conceptualization.

Funding

This work was supported by the Slovenian Research and Innovation Agency (ARIS) research core funding No. P2-0095, and the HEDGE-IoT project, which has received funding from the European Union's Horizon Europe research and innovation programme under grant agreement No. 101136216.

Declaration of competing interest

The authors declare that they have no known competing financial interests or personal relationships that could have appeared to influence the work reported in this paper.

Acknowledgements

Authors would like to express our gratitude to the Slovenian TSO, ELES, Ltd. and Janko Kosmač for providing the data required for this study.

Data availability

Data used in this study will be made available on request.

References

[1] Innovation landscape for a renewable-powerede future: Solutions to integrate variable renewables. 2019.
[2] Das O, Zafar MH, Sanfilippo F, Rudra S, Kolhe ML. Advancements in digital twin technology and machine learning for energy systems: A comprehensive review of applications in smart grids, renewable energy, and electric vehicle optimisation. Energy Convers Manag: X 2024;24:100715. http://dx.doi.org/10.1016/j.ecmx.2024.100715.
[3] Maroufkhani P, Desouza KC, Perrons RK, Iranmanesh M. Digital transformation in the resource and energy sectors: A systematic review. Resour Policy 2022;76:102622. http://dx.doi.org/10.1016/j.resourpol.2022.102622.
[4] Cimini Jr CA, Fonseca BQA. Temperature profile of progressive damaged overhead electrical conductors. Int J Electr Power Energy Syst 2013;49:280–6.
[5] A. Douglass D, Grant I, Jardini JA, Kluge R, Traynor P, Davis C, Gentle J, Nguyen H-M, Chisholm W, Xu C, Goodwin T, Chen H, Nuthalapati S, Hurst N. A Review of Dynamic Thermal Line Rating Methods With Forecasting. IEEE Trans Power Deliv 2019;34(6):2100–9. http://dx.doi.org/10.1109/TPWRD.2019.2932054.
[6] Maksić M, Djurica V, Souvent A, Slak J, Depolli M, Kosec G. Cooling of overhead power lines due to the natural convection. Int J Electr Power Energy Syst 2019;113:333–43. http://dx.doi.org/10.1016/j.ijepes.2019.05.005, Publisher: Elsevier.
[7] Guide for thermal rating calculations of overhead lines. Guide. CIGRE; 2014.
[8] IEEE Standard for Calculating the Current-Temperature Relationship of Bare Overhead Conductors, IEEE Std 738™-2023. IEEE; 2023.
[9] Dynamic line rating - innovation landscape brief. 2020.
[10] Matus M, Sáez D, Favley M, Suazo-Martínez C, Moya J, Jiménez-Estévez G, Palma-Behnke R, Olguín G, Jorquera P. Identification of critical spans for monitoring systems in dynamic thermal rating. IEEE Trans Power Deliv 2012;27(2):1002–9.
[11] Abboud AW, Gentle JP, McJunkin TR, Lehmer JP. Using computational fluid dynamics of wind simulations coupled with weather data to calculate dynamic line ratings. IEEE Trans Power Deliv 2020;35(2):745–53. http://dx.doi.org/10.1109/TPWRD.2019.2925520.
[12] Hosek J, Musilek P, Lozowski E, Pytlak P. Effect of time resolution of meteorological inputs on dynamic thermal rating calculations. IET Gener Transm Distrib 2011;5(9):941. http://dx.doi.org/10.1049/iet-gtd.2011.0039.
[13] Howington BS, Ramon GJ. Dynamic thermal line rating summary and status of the state-of-the-art technology. IEEE Trans Power Deliv 1987;2(3):851–8. http://dx.doi.org/10.1109/TPWRD.1987.4308190.
[14] Karimi S, Musilek P, Knight AM. Dynamic thermal rating of transmission lines: A review. Renew Sustain Energy Rev 2018;91:600–12. http://dx.doi.org/10.1016/j.rser.2018.04.001.
[15] Poli D, Pelacchi P, Lutzemberger G, Baffa Scirocco T, Bassi F, Bruno G. The possible impact of weather uncertainty on the dynamic thermal rating of transmission power lines: A Monte Carlo error-based approach. Electr Power Syst Res 2019;170:338–47. http://dx.doi.org/10.1016/j.epsr.2019.01.026.
[16] Rashkovska A, Jančič M, Depolli M, Kosmač J, Kosec G. Uncertainty assessment of dynamic thermal line rating for operational use at transmission system operators. IEEE Trans Power Syst 2022;37(6):4642–50. http://dx.doi.org/10.1109/TPWRS.2022.3144740.
[17] Chen Z, Zhang B, Du C, Li P, Meng W. Secure probabilistic interval prediction of dynamic thermal rating against weather imbalance constraints. IEEE Trans Ind Informat. 2024;20(10):12375–84. http://dx.doi.org/10.1109/TII.2024.3423408.
[18] Pytlak P, Musilek P, Lozowski E, Toth J. Modelling precipitation cooling of overhead conductors. Electr Power Syst Res 2011;81(12):2147–54. http://dx.doi.org/10.1016/j.epsr.2011.06.004.
[19] Kosec G, Maksić M, Djurica V. Dynamic thermal rating of power lines – model and measurements in rainy conditions. Int J Electr Power Energy Syst 2017;91:222–9. http://dx.doi.org/10.1016/j.ijepes.2017.04.001.
[20] Suomi I, Vihma T. Wind gust measurement techniques—From traditional anemometry to new possibilities. Sensors 2018;18(4). http://dx.doi.org/10.3390/s18041300.
[21] El Rafei M, Sherwood S, Evans J, Dowdy A. Analysis and characterisation of extreme wind gust hazards in new south Wales, Australia. Nat Hazards 2023;117:1–21. http://dx.doi.org/10.1007/s11069-023-05887-1.
[22] Raichle BW, Carson WR. Wind resource assessment of the southern appalachian ridges in the southeastern United States. Renew Sustain Energy Rev 2009;13(5):1104–10.
[23] Yang X, Tao Y, Jin Y, Ye B, Ye F, Duan W, Xu R, Zeng Z. Time resolution of wind speed data introduces errors in wind power density assessment. Energy Convers Manag: X 2024;24:100753. http://dx.doi.org/10.1016/j.ecmx.2024.100753.
[24] Rott A, Doekemeijer B, Seifert JK, van Wingerden J-W, Kühn M. Robust active wake control in consideration of wind direction variability and uncertainty. Wind Energy Sci 2018;3(2):869–82. http://dx.doi.org/10.5194/wes-3-869-2018.
[25] Houle J, van Breugel F. Near-surface wind variability over spatiotemporal scales relevant to plume tracking insects. Phys Fluids 2023;35(5):055145. http://dx.doi.org/10.1063/5.0147945.

[26] Shu Z, Chan P, He X. Analysis of horizontal wind direction variability considering different influencing factors. J Wind Eng Ind Aerodyn 2024;252:105819. http://dx.doi.org/10.1016/j.jweia.2024.105819.
[27] Mahrt L. Surface wind direction variability. J. Appl Meteorol Climatology 2011;50(1):144–52. http://dx.doi.org/10.1175/2010JAMC2560.1.
[28] Guide to Instruments and Methods of Observation, Volume I - Measurement of Meteorological Variables. World Meteorological Organization; 2023.
[29] Gilhousen DB. A field evaluation of NDBC Moored buoy winds. J. Atmospheric Ocean Technol. 1987;4(1):94–104. http://dx.doi.org/10.1175/1520-0426(1987)004<0094:AFEONM>2.0.CO;2.
[30] Thomas BR, Swail VR. Buoy wind inhomogeneities related to averaging method and anemometer type: application to long time series. Int J Climatol 2011;31(7):1040–55. http://dx.doi.org/10.1002/joc.2339.
[31] How to average winds? | Copernicus Marine Help Center. URL https://help.marine.copernicus.eu/en/articles/5487266-how-to-average-winds.
[32] Ward KR, Bamisile O, Ejiyi CJ, Staffell I. Time-averaged wind power data hides variability critical to renewables integration. Energy Strat Rev 2023;50:101235. http://dx.doi.org/10.1016/j.esr.2023.101235.
[33] González-Cagigal M, Rosendo-Macías J, Bachiller-Soler A, Señas-Sanvicente D. Influence of the wind variability on the calculation of dynamic line rating. Electr Power Syst Res 2022;211:108234. http://dx.doi.org/10.1016/j.epsr.2022.108234.